Electrodeposited metallic glasses with superlative wear resistance

Mayur Pole, Maryam Sadeghilaridjani, Jibril Shittu, Chaitanya Mahajan, Nandita Ghodki, Sundeep Mukherjee [*]

Department of Materials Science and Engineering, University of North Texas, Denton, TX, 76203, USA

ABSTRACT

The electrodeposition route to obtain amorphous alloys offers a facile, low-cost, and versatile alternative to conventional melt quenching. However, there are significant knowledge gaps in tribological properties and wear mechanisms for electrodeposited metallic glasses (EMGs). Here, the wear behavior and the scratch response of a model binary amorphous alloy system were investigated. Electrodeposited Ni–P metallic glasses were systematically studied as a function of composition, with amorphous alloy formation over the narrow range of 10 at% to 20 at% phosphorus. The electrodeposited metallic glasses showed hardness values in the range of 6.6–7.4 GPa, modulus in the range of 155–163 GPa, and friction coefficient around 0.50. Among the studied alloys, electrodeposited $Ni_{80}P_{20}$ showed the lowest wear rate, which was two orders of magnitude lower than electrodeposited pure Ni. The wear mechanism was determined to be extensive plastic deformation along with mild ploughing, micro tears, and formation of discontinuous lubricious oxide patches. Scratch tests showed an increase in critical load for damage initiation with the increase in phosphorus content among the amorphous alloys following the trend: $Ni_{80}P_{20} > Ni_{85}P_{15} > Ni_{90}P_{10}$. The overall wear rate for the electrodeposited metallic glasses was found to be lower than most reported bulk metallic glasses (BMGs). This represents a fundamental study on structure-property correlations in electrodeposited metallic glasses and demonstrates the versatility of electrodeposition in tuning the surface properties of amorphous alloys.

1. Introduction

Metallic glasses (MGs) show a range of very attractive properties including ultra-high strength, hardness, and excellent corrosion and wear resistance for use in structural and functional applications [1–4]. Their superior surface degradation resistance makes them appealing for applications ranging from bioimplants to bearings and gears [5–9]. Compared to the typical route of rapid melt quenching, we have recently demonstrated that electrodeposition is a facile, scalable, and cost-effective approach to synthesize amorphous alloys across multiple length-scales [10,11]. A range of alloys may be obtained by tactical control of electrolyte composition, temperature, pH, and deposition current density. However, there are few reports and limited understanding of the tribological properties and wear mechanisms for electrodeposited metallic glasses (EMGs).

A wide range of electrodeposited alloys have been considered as alternatives to conventional hard chromium coatings that have been shown to adversely impact the environment and human health [12–14]. Among these, Ni–P alloys have attracted much attention because of their

high hardness as well as excellent wear and corrosion resistance [15,16]. Wear behavior of electroless and electrodeposited Ni–P, and their composites have been reported [17,18]. Tribological studies on electroless Ni–P, Ni–W–P, and Ni–P–Al$_2$O$_3$ alloys showed that the presence of secondary hard particles significantly improves wear resistance even at elevated temperatures [17,18]. Graded Ni–P alloys obtained by electrodeposition exhibited higher hardness and lower wear rates compared to hard Cr coatings [19]. In the form of a composite microstructure, Ni–P with nano-TiO$_2$ showed very low wear rates [20]. However, there are no systematic studies on the wear and scratch behavior of electrodeposited metallic glasses as a function of composition. In addition, there is limited understanding of the failure mechanisms as a function of applied load and reciprocation frequency.

Here, the wear behavior and scratch response of $Ni_{100-x}P_x$ (x = 0, 10, 15, and 20 at%) alloys synthesized using pulsed electrodeposition technique were studied. Alloys synthesized by pulsed current (PC) electrodeposition technique usually have less internal (residual) stresses and defect density compared to electroless deposition, which significantly enhance their tribological properties [21]. In addition, pulsed

---

* Corresponding author.
E-mail address: sundeep.mukherjee@unt.edu (S. Mukherjee).

electrodeposition allows precise control of alloy chemistry and microstructure not achievable with direct current (DC) plating [22,23]. The microstructure, friction, wear, and scratch behavior of $Ni_{100-x}P_x$ electrodeposited alloys were investigated as a function of applied load and sliding frequency. The damage mechanism was studied in detail and compared with bulk metallic glasses (BMGs). These findings pave the way for enhancement in tribological properties of electrodeposited metallic glasses by tuning their structure and composition.

2. Materials and methods

2.1. Alloy synthesis

$Ni_{100-x}P_x$ (x = 0, 10, 15, and 20 at. %) alloys were electrodeposited on commercial pure copper plates using a pulse power supplier (Dynatronix-MicroStar) in a modified Watt's bath containing phosphorous acid (H_3PO_3 (20 g/L)) with nickel sulfate ($NiSO_4 \cdot 6H_2O$ (365 g/L)), nickel chloride ($NiCl_2 \cdot 6H_2O$ (32 g/L)), boric acid (H_3BO_3 (40 g/L)), and sodium dodecyl sulfate ($NaC1_2H_{25}SO_4$ (0.4 g/L)) as electrolytes. Pure nickel coating was obtained in the absence of H_3PO_3. The substrates were mechanically polished to mirror surface finish and cleaned ultrasonically in acetone for 10 min followed by distilled water washing. The applied pulse frequency and duty cycle were 100 Hz and 0.5, respectively. The temperature of the bath was set to ~40 °C and pH was selected as 1.8 and were regulated during the deposition to avoid composition variation over long periods of time. Peak current density was adjusted in the range of 5–20 A/dm^2 with a deposition time ranging from 30 min to 240 min to obtain the desired compositions.

2.2. Structural characterization and thermal analysis

The structure of the alloys was determined using X-ray diffraction (XRD, Rigaku Ultima X-ray diffractometer) with 1.54 Å Cu-Kα radiation. The sample was cut, and the thickness and the elemental distribution were characterized using scanning electron microscopy (SEM, FEI Quanta-ESEM 200) equipped with energy dispersive spectroscopy (EDS). Thermal analysis of the electrodeposited metallic glasses was performed using differential scanning calorimetry (DSC) (NETZSCH DSC 404C) at a constant heating and cooling rate of 20 °C/min.

2.3. Mechanical and tribological properties

Hardness and modulus measurements of the electrodeposited alloys were obtained using TI-Premier nano-indenter (Bruker, Minneapolis, MN, USA) with a diamond Berkovich tip at room temperature and peak load of 1 N. An array of 4 × 4 indents was used with 100 μm spacing between two indents to obtain the average and standard deviation. By Hertzian theory of contact mechanics, the nano-indentation technique may be used to calculate the reduced modulus (E_r) according to equation (1) and the Young's modulus of the sample (Es) according to equation (2) as:

$$E_r = \frac{\sqrt{\Pi}}{2} \frac{S}{\sqrt{A_c}} \tag{1}$$

$$\frac{1}{E_r} = \frac{(1 - v_s^2)}{E_s} + \frac{(1 - v_i^2)}{E_i} \tag{2}$$

where, S is the slope of unloading curve at maximum depth, A_c is the contact area of the indenter at maximum depth, v_s is the Poisson's ratio of the sample *(~0.31)* [24], v_i is the Poisson's ratio of the diamond indenter (0.07), and E_i is the Young's modulus of the diamond indenter.

Dry sliding and reciprocating wear tests were performed using RTEC Universal Reciprocating Tribometer. AISI 52100 balls, 6 mm in diameter, were used as counterface material. Tests were conducted in ambient air (~22% RH) under a normal load of 1 N, 5 N, and 10 N at frequency of 5 Hz. Reciprocating frequencies of 1 Hz, 5 Hz, and 10 Hz were used at a load of 5 N to investigate the effect of frequency. The wear behavior was characterized for a total time of 60 min with 3.5 mm stroke length corresponding to 126 m of sliding distance to evaluate steady-state friction as a function of normal load. MFT17 software was used to record the tangential load, which determines the coefficient of friction (COF), and the wear tracks were analyzed using white light interferometry (WLI) at 10× magnification. 3D profiles of the wear tracks were stitched and analyzed to calculate the wear volume loss (mm^3) using Gwyddion software. Wear rates (mm^3/N.m) were calculated by dividing wear volume loss with load and the sliding distance. At least three tests were carried out for each condition and the average value was reported. Wear tracks were characterized using SEM to evaluate the wear mechanism.

Unidirectional scratch tests of 10 mm length were performed using the RTEC instruments tribometer with a Rockwell diamond stylus having a tip angle of 120° with a 200 μm radius. The lateral displacement speed and loading rate were chosen as 6 mm/min and 100 N/min, respectively. Progressive increasing load tests in the range of 5 N–180 N were conducted for each alloy and variation in COF was recorded. The displacement corresponding to the onset of failure was identified using SEM. The critical load for damage initiation (L_C), which is a measure of the cohesive strength, was calculated from progressive load experiment as [25]:

$$L_C = [L_{rate} \times (l_c / X_{rate})] + L_{start} \tag{3}$$

where, L_{rate} is the loading rate (N/min), l_c is the distance in mm between the start of the scratch track and starting point of damage in the scratch scar, X_{rate} is the rate of horizontal displacement (mm/min), and L_{start} is the preload established at the start of the scratch test. For each alloy, the average value was obtained from five separate tests.

3. Results and discussion

3.1. Microstructural characterization

Fig. 1(a) shows a representative cross-section SEM image of one of the electrodeposited alloys, namely $Ni_{80}P_{20}$, on Cu substrate. The deposited alloy was clean, smooth, and free from pores and defects. All the other electrodeposited alloys showed very similar characteristics with an average thickness in the range of ~35–50 μm. Elemental composition of the alloys was determined using EDS and shown in Fig. 1 (b) indicating homogeneous distribution of the constituent elements. The average compositions were determined to be Ni, $Ni_{90}P_{10}$, $Ni_{85}P_{15}$, and $Ni_{80}P_{20}$ with variation of less than 0.5 at%. XRD spectrum for all the electrodeposited alloys are shown in Fig. 1(c). Electrodeposited pure Ni showed peaks corresponding to face centered cubic (FCC) crystal structure. For phosphorous content in the range of 10–20 at. %, a broad diffraction peak was seen at 2θ in the range of 35°-55° indicating fully amorphous structure. For phosphorus content less than 10 at. % and more than 20 at. %, several sharp crystalline peaks were seen (not included here for clarity) indicating amorphous alloy formation only in the narrow composition range of 10–20 at. %P. DSC curves for the three electrodeposited metallic glasses, namely $Ni_{90}P_{10}$, $Ni_{85}P_{15}$, and $Ni_{80}P_{20}$, are shown in Fig. 1(d). The glass transition temperature (T_g) was found to be in the range of 310–315 °C and crystallization temperature (T_x) was in the range of 340–350 °C with the crystallization peak becoming broader for the alloys with higher phosphorus content. A broad endothermic peak indicating glass transition was seen before the sharp exothermic crystallization peak as shown in the inset of Fig. 1(d).

3.2. Hardness, modulus, friction, and wear rate

Hardness and modulus for the Ni–P EMGs were determined by nano-indentation using a peak load of 1 N and the corresponding load versus
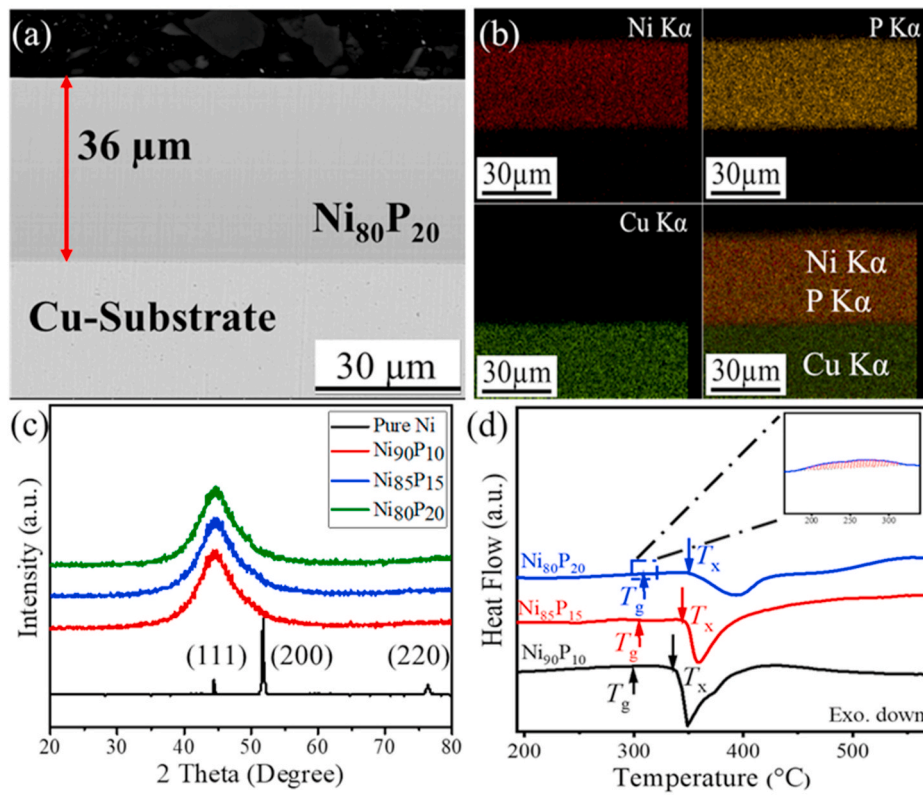
Fig. 1. (a) Cross-section SEM image of electro-deposited $Ni_{80}P_{20}$ alloy showing uniform and smooth surface with average thickness of ~36 μm; (b) cross-section EDS map of $Ni_{80}P_{20}$ alloy indicating uniform distribution of Ni and P; (c) XRD plot for the electrodeposited Ni–P alloys showing transition from pure crystalline Ni to amorphous $Ni_{90}P_{10}$, $Ni_{85}P_{15}$, and $Ni_{80}P_{20}$ alloys; (d) DSC plot for the three electrodeposited Ni–P metallic glasses at 20 °C/min with glass transition temperature (T_g) with an inset figure indicating glass transition phenomena, and crystallization temperature (T_x) shown alongside the curves.

displacement curves are shown in Fig. 2(a). For the same peak load of 1 N, the displacement decreases in the order of Ni > $Ni_{90}P_{10}$ > $Ni_{85}P_{15}$ > $Ni_{80}P_{20}$. The peak load was selected to keep the maximum indentation depth to less than 3 μm to avoid any potential substrate effect. The relative degree of indentation depth indicates that hardness follows the trend: $Ni_{80}P_{20}$ > $Ni_{85}P_{15}$ > $Ni_{90}P_{10}$ > Ni. Among the EMGs, the load-displacement curves for $Ni_{85}P_{15}$ and $Ni_{80}P_{20}$ alloys showed

pronounced degree of serrations (or pop-ins) in contrast to the smooth curve for $Ni_{90}P_{10}$ as shown by the magnified view in Fig. 2(b). Serrated deformation behavior in metallic glasses is associated with shear band nucleation for local accommodation of plastic strain [26]. High density of pop-ins or serrations for $Ni_{85}P_{15}$ and $Ni_{80}P_{20}$ indicates localized deformation and brittle behavior in contrast to $Ni_{90}P_{10}$ EMG, which showed smooth deformation indicative of relatively more ductile
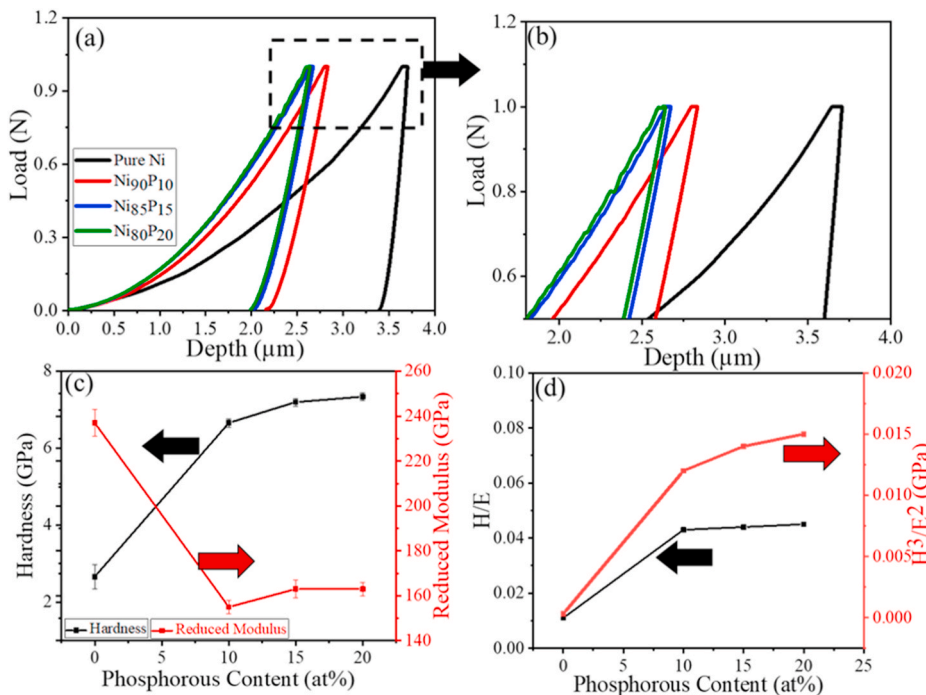

Fig. 2. (a) Nano-indentation load-displacement curves for pure Ni and Ni–P electrodeposited alloys; (b) high-magnification view of the selected region in (a) showing serrated behavior for $Ni_{85}P_{15}$ and $Ni_{80}P_{20}$ in contrast to smooth curves for $Ni_{90}P_{10}$ and Ni; (c) hardness and reduced modulus as a function of phosphorus content for the electrodeposited alloys indicating higher hardness and lower modulus for the metallic glasses compared to pure Ni; (d) H/E and H^3/E^2 ratios as a function of phosphorus content for the electrodeposited alloys showing higher values for the metallic glasses compared to pure Ni.

behavior [27]. The average hardness increased with increase in phosphorous content as shown in Fig. 2(c). The Ni–P EMGs showed almost a three-fold higher hardness (H) but lower modulus (E) compared to electrodeposited pure Ni. The modulus for the EMGs was about 30% lower compared to that of crystalline Ni due to relatively lower bond strength and less dense packing in the amorphous structure compared to its crystalline counterpart [28]. Among the amorphous alloys, a small increase in modulus was seen with increase in phosphorus content. This may be attributed to more short range ordering and bicapped square antiprism (BSAP) atomic clusters with increase in the metalloid content, as we demonstrated recently [10]. H/E is a measure of the limit of elastic behavior in a surface contact and H^3/E^2 dictates the resistance to plastic deformation of materials in loaded contact [29,30]. H/E and H^3/E^2 ratios increased with increase in phosphorus content as shown in Fig. 2 (d). Materials with higher values of H/E and H^3/E^2 ratios typically show better elastic recovery and higher wear resistance under dynamic loading [31–35]. The average hardness (H), modulus (E), H/E, and H^3/E^2 values for all the electrodeposited alloys are summarized in Table 1.

The average coefficient of friction for the electrodeposited alloys sliding against AISI 52100 steel counterface at frequency of 5 Hz as a function of load (1 N, 5 N and 10 N) is shown in Fig. 3(a). The COF increased with increase in load from 1 N to 5 N and remained roughly unchanged for increase in load from 5 N to 10 N for all the alloys. The increase in COF may be attributed to mechanical instability of the oxides formed leading to increase in material removal rate at higher load [36–38]. Fig. 3(b) shows the COF for all alloys as a function of sliding frequency at a normal load of 5 N. The average COF was in the range of 0.45–0.5 for the three EMGs, which was 15–25% lower than electrodeposited pure Ni (~0.6) irrespective of sliding frequency. All the alloys showed a slight increase in COF at 5 Hz which may be attributed to change in contact area and severe plastic deformation on the contact surface creating more asperity junctions [37,39]. In contrast, Ni based BMGs showed an increase in frictional force with increase in contact pressure indicating an increase in COF with load [40]. Fig. 3(c) and (d) show the 2-dimensional (2D) wear track cross-section profile for pure Ni and the Ni–P electrodeposited alloys at the loads of 1 N and 10 N at 5 Hz reciprocation frequency. The wear width and depth decreased with increase in phosphorous content at low load (Fig. 3(c)), which may be due to the higher H/E and H^3/E^2 values that reduce the contact pressure upon sliding. The saw-tooth cross section profiles may be attributed to elimination of wear debris and localized fractures in the wear tracks. With increase in load to 10 N, the wear scar cross-section width and depth increased due to higher contact stresses and the Ni–P amorphous alloys showed significantly smaller wear volume compared to pure Ni (Fig. 3(d)). The 2D wear track cross-section profiles for pure Ni and Ni–P alloys at frequencies of 1 Hz and 10 Hz at 5 N load are shown in Fig. 3(e) and (f). The wear scar dimensions decreased with increase in reciprocation frequency, which may be attributed to the formation of oxide film at higher frequency that reduced metal-metal contact. Fig. 3(g) and (h) show the wear rates for the electrodeposited alloys as a function of normal load and frequency, respectively. Pure Ni showed significantly higher wear rates compared to the Ni–P EMGs, particularly at higher

loads and higher frequencies of reciprocation. Higher wear rate with increase in load may be attributed to large plastic deformation or delamination with the formation of asperities [41]. Among the EMGs, wear rate decreased in the following order: $Ni_{90}P_{10} > Ni_{85}P_{15} > Ni_{80}P_{20}$. This is attributed to the increase in hardness (H), H/E, and H^3/E^2 values with higher phosphorus content. The wear rate decreased with increase in sliding frequency for all the alloys (Fig. 3(d)), which may be because of the increase in frictional heat and formation of tribo-layer and transfer layer leading to self-lubrication from the decreased metal-metal contact. With the increase in phosphorus content, bicapped square antiprism (BSAP) atomic clusters tends to increase resulting in strong network structure, which can lead to higher hardness and modulus [10]. This likely explains the lowest wear rates for $Ni_{80}P_{20}$ both as a function of load and sliding frequency.

3.3. Wear mechanism as a function of load and frequency

Fig. 4 shows SEM images of the wear tracks on electrodeposited Ni and Ni–P alloys as a function of different loads against AISI 52100 counterface. Fig. 4(a–c) show the SEM images of the wear tracks for electrodeposited Ni as a function of load. At the low load of 1 N, electrodeposited Ni exhibited a combination of micro grooves, plastic deformation and delamination resulting in abrasive wear. With increase in load, ploughing was reduced and there were signs of more adhesive wear and delamination which became more prominent at the highest load of 10 N. The increase in contact stress resulted in a transition from abrasive wear to severe delamination, which explains the monotonic increase in wear rate for Ni as a function of load. EDS analysis (Supplementary Table S1) showed an increase in oxygen content on the wear scar with increase in normal load. Fig. 4(d–f) show the SEM images of wear scars on $Ni_{90}P_{10}$ as a function of load. The extent of plastic deformation was less at the minimum load with shallow grooves, mild delamination on the surface and starting signs of decohesion and cracking of the oxide layer. At the highest load of 10 N, the extent of plastic deformation increased with dense cracks on the surface oxide layer. No third body abrasion was seen at the higher loads supporting the lowest wear rate for $Ni_{90}P_{10}$ at 10 N load. Supplementary Table S2 shows increase in oxygen content on the wear scar with increase in normal load for $Ni_{90}P_{10}$ indicating oxidative wear at the higher loads. Fig. 4(g–i) show the SEM images of wear tracks for $Ni_{85}P_{15}$ as a function of load. Similar kind of behavior was seen for this alloy, showing minimal plastic deformation at lower loads with fine wear debris resulting in micro ploughing and partial abrasive wear. Formation of discontinuous tribo-layer and cracks in the oxide layer were also seen. Presence of constituent elements and oxygen partition on the wear track (summarized in Supplementary Table S3) indicates partial oxidative wear for $Ni_{85}P_{15}$. At 10 N load, extensive plastic deformation was seen on the wear scar with increase in contact area. Formation of oxide layer with micro shear cracks were also observed on the scar at high load. The oxygen content did not change significantly with increase in load for $Ni_{85}P_{15}$ as shown in Supplementary Table S3. SEM images of wear tracks for $Ni_{80}P_{20}$ as a function of load are shown in Fig. 4(j–l). At low load of 1 N, there was a combination of abrasive wear with deep grooves and plastic deformation on the scar as well as discontinuous tribo-layer formed on the wear track. The extent of plastic flow increased, and the degree of abrasion decreased with increase in applied stress for $Ni_{80}P_{20}$ electrodeposited alloy. In addition, the oxide layer formed on the surface did not undergo severe cracking with increase in load, which may be attributed to the higher H/E and H^3/E^2 ratios for this alloy. Supplementary Table S4 shows high oxygen content in the wear track of $Ni_{80}P_{20}$ tested at 10 N, which may be attributed to the relatively higher temperature rise in the contact area for this alloy. Similar signs of plastic deformation, grooving, and pile-up around the wear track were observed for Ni based BMGs [42]. In contrast, Zr based BMGs showed shear mediated adhesive wear, where plastic deformation and ploughing were less pronounced [43].

Table 1
Nano-mechanical and scratch properties of all the electrodeposited alloys.

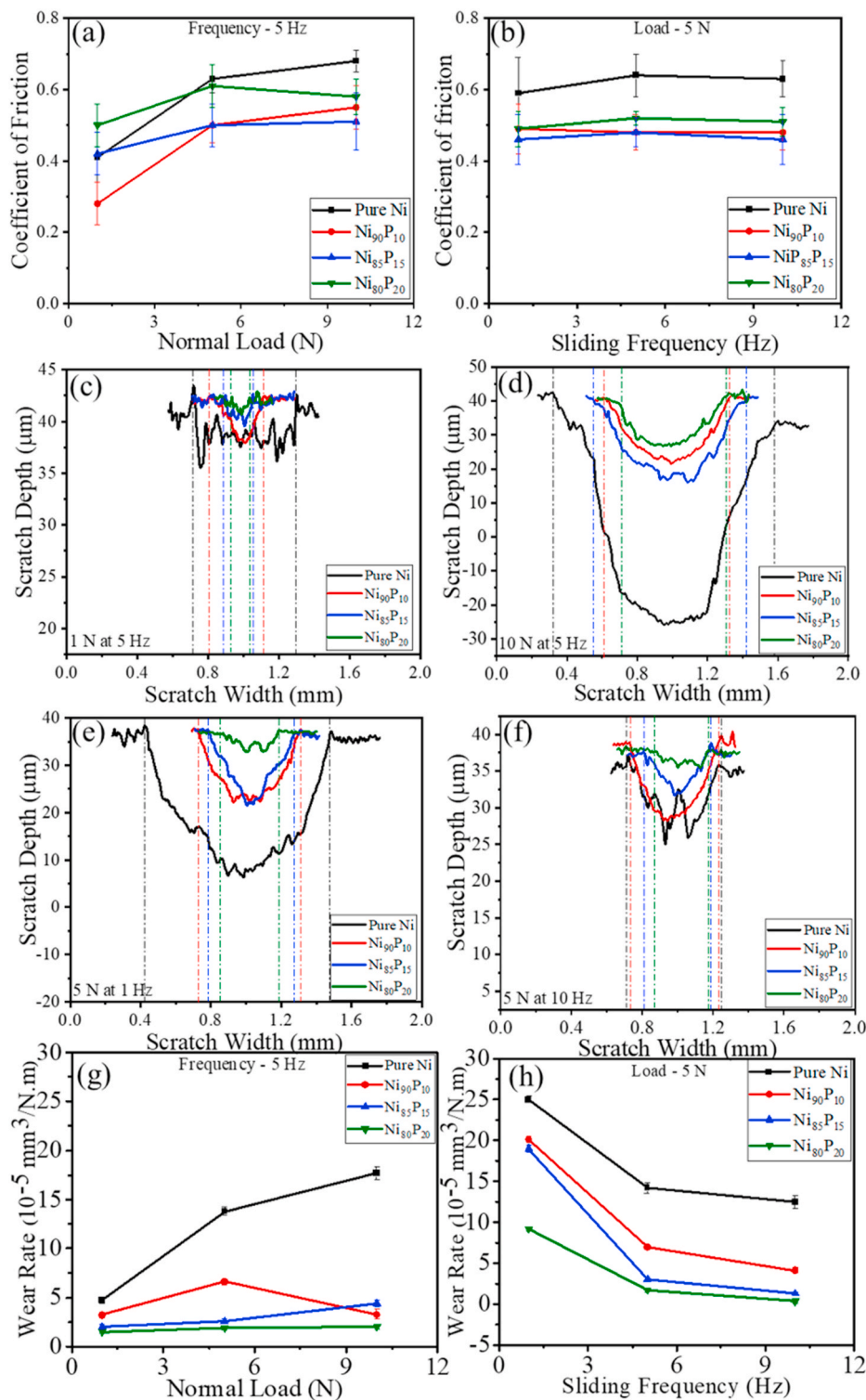| Alloys	H (GPa)	E$_r$ (GPa)	H/E	H^3/E^2 (GPa)	Critical Load for Initial Failure (N)
Ni	2.66 ± 0.35	237 ± 6	0.011	0.0003	43 ± 3
Ni$_{90}$P$_{10}$	6.66 ± 0.11	155 ± 3	0.043	0.012	53 ± 3
Ni$_{85}$P$_{15}$	7.20 ± 0.10	163 ± 4	0.044	0.014	58 ± 2
Ni$_{80}$P$_{20}$	7.34 ± 0.10	163 ± 3	0.045	0.015	62 ± 4

Fig. 3. Average coefficient of friction for electrodeposited Ni and Ni–P electrodeposited metallic glasses as a function of (a) normal load at 5 Hz reciprocation frequency and (b) sliding frequency at 5 N load; (c, d) wear track cross-section profiles at normal loads of 1 N and 10 N at 5 Hz frequency; (e, f) wear track cross-section profiles at sliding frequencies of 1 Hz and 10 Hz at 5 N load; (g) wear rate as a function of normal load at 5 Hz reciprocation frequency; (h) wear rate as a function of sliding frequency at 5 N normal load.

SEM images of the wear scars on the electrodeposited alloys against AISI 52100 counterface at different sliding frequencies are shown in Fig. 5. SEM images of the wear tracks for electrodeposited Ni are shown in Fig. 5(a–c). The wear scar exhibited extensive material removal with abrasive grooves and severe delamination in the sample at 1 Hz, as shown in Fig. 5(a). With increase in reciprocation frequency, there was decrease in the extent of delamination and wear rate with corresponding change in mechanism to oxidative wear. Supplementary Table S5 clearly illustrates the change in mechanism to oxidative wear with increase in

oxygen fraction on the wear track with increase in sliding frequency. Fig. 5(d–f) show the SEM micrographs of the wear track for $Ni_{90}P_{10}$ alloy as a function of sliding frequency varied from 1 Hz to 10 Hz. Abrasive grooves, plastic deformation, and extensive material removal was seen for the wear scars at lower frequency indicating abrasive wear mechanism. Increased metal-counterface contact led to high wear rate at low frequency. With increase in sliding frequency, the extent of micro grooves and severe deformation of the wear surface decreased with the formation of discontinuous tribo-layer that acted as a lubricious surface
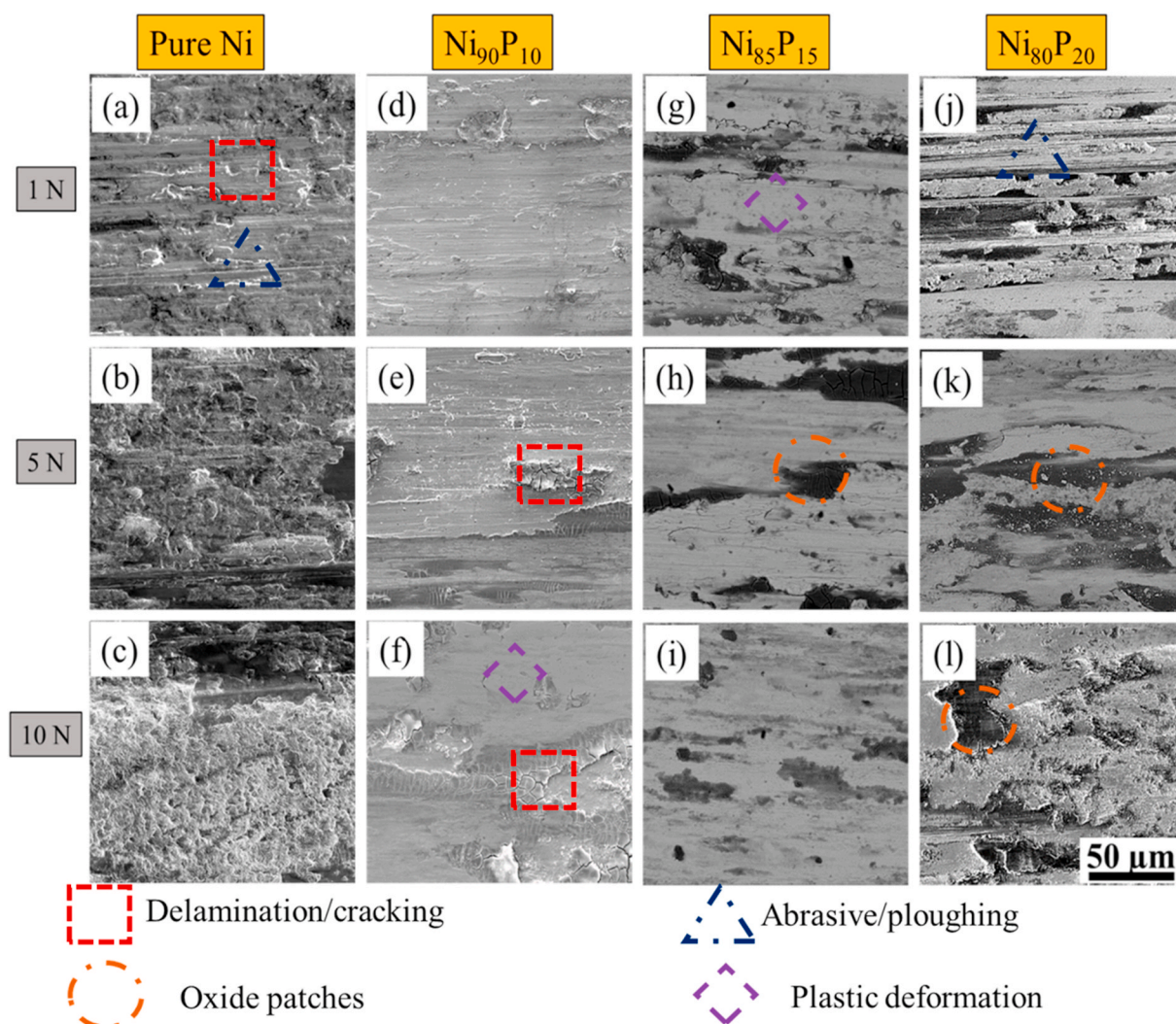
Fig. 4. SEM images of wear tracks at 5 Hz corresponding to 126 m of sliding distance as a function of normal load for (a-c) pure Ni, (d-f) $Ni_{90}P_{10}$, (g-i) $Ni_{85}P_{15}$ and (j-l) $Ni_{80}P_{20}$. Pure Ni showed a transition from mild abrasive wear and plastic deformation at low load to delamination and extensive deformation at high load. $Ni_{90}P_{10}$ and $Ni_{85}P_{15}$ showed abrasive wear at low load and deformation with discontinuous oxide patches at the higher loads. $Ni_{80}P_{20}$ electrodeposited alloy showed abrasive wear with plastic deformation at low load and mild abrasive wear with discontinuous oxide patches at the higher loads.

lowering the overall wear rate. EDS analysis confirmed the increase in oxygen content with increase in sliding frequency (Supplementary Table S6). Similar wear mechanisms were seen for $Ni_{85}P_{15}$ electrodeposited alloy as shown in Fig. 5(g–i). At 1 Hz frequency, $Ni_{85}P_{15}$ exhibited high material removal rate with abrasive grooves and agglomerated wear debris (shown in Fig. 5(g)) which contributed to high wear rate. With increase in frequency to 5 Hz, formation of discontinuous oxide layer increased with finer wear debris and cracks (Fig. 5(h)) resulting in decreased wear rate as shown in Fig. 3(d). At 10 Hz frequency, the $Ni_{85}P_{15}$ alloy showed very fine micro grooves, fine deformation of the surface, oxide layer with minimal cracks and very fine micro tears on the tribo-layer. The EDS results, summarized in Supplementary Table S7, confirmed the increase in oxygen content on the wear scar indicating a transition in wear mechanism from abrasive wear to oxidative wear. SEM micrographs of the wear tracks for $Ni_{80}P_{20}$ EMG at different sliding frequencies are shown in Fig. 5(j–l). At 1 Hz frequency, material removal from the wear track was in the form of small adhesive patches and mild abrasive wear was observed with cracked oxide patches as shown in Fig. 5(j). Similar behavior was seen at 5 Hz with relatively more cracked oxide layer (Fig. 5(k)). At 10 Hz frequency, the wear track exhibited very small pores indicating mild abrasive wear with discontinuous tribo-layer. EDS analysis of the wear

scar for $Ni_{80}P_{20}$ is summarized in Supplementary Table S8 confirming the increase in oxygen content with increase in sliding frequency.

3.4. Scratch behavior and critical load for cohesive failure

Coefficient of friction (COF) was evaluated for the electrodeposited alloys as a function of normal load by progressive scratch tests (Supplementary Fig. 1). The COF reached steady state at a load of ~60 N and was in the range of ~0.35–0.45 for all the alloys after showing fluctuations during the initial stage of loading possibly due to surface roughness of the deposited alloys. Absence of a large drop or spike in the COF curve for each of the alloys indicated that the progressive scratch did not reach the substrate till the final load. The critical load for cohesive failure was calculated by measuring the length from the starting point of the scratch to the crack initiation point. Fig. 6 shows the SEM images of the progressive scratch test for each of the alloys. The critical length for damage initiation (l_c) is marked for each of the alloys, which increased with increase in phosphorus content. Supplementary Figures 2 through 4 show the SEM images of the progressive scratch for $Ni_{90}P_{10}$, $Ni_{85}P_{15}$, and $Ni_{80}P_{20}$ electrodeposited alloys with zoomed in view showing the region separating the damaged from the undamaged sections highlighted with dashed yellow lines as a guide to the eye. For
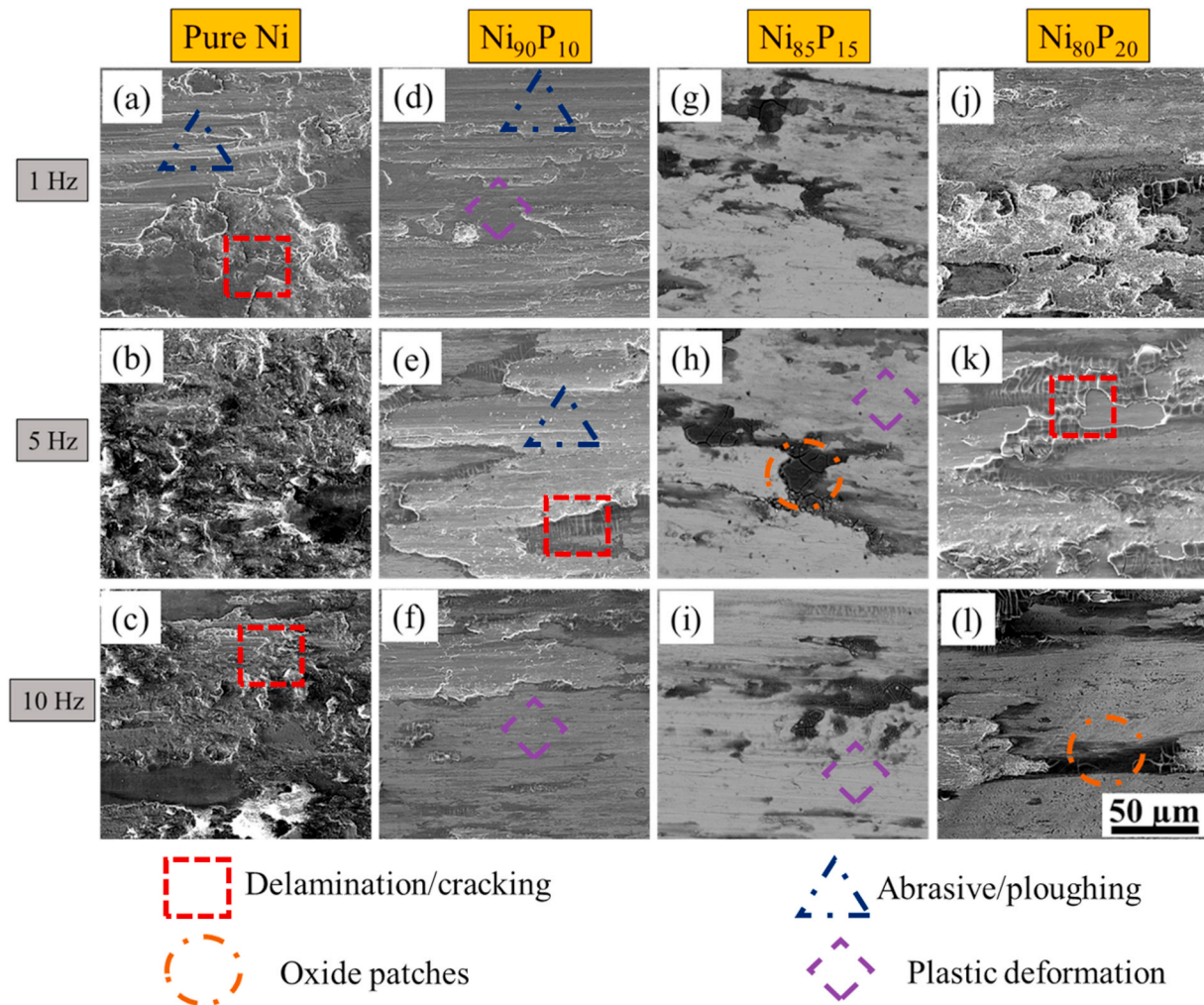
Fig. 5. SEM images of wear tracks at 5 N load corresponding to 12.6 m, 63 m, and 126 m of sliding distances as a function of sliding frequency for (a–c) pure Ni, (d–f) $Ni_{90}P_{10}$, (g–i) $Ni_{85}P_{15}$ and (j–l) $Ni_{80}P_{20}$. Pure Ni showed a transition from abrasive wear at low frequency to oxidative wear at the higher frequencies. $Ni_{90}P_{10}$, and $Ni_{85}P_{15}$ showed abrasive wear with mild deformation at low frequency and partial oxidative wear at the higher frequencies. $Ni_{80}P_{20}$ electrodeposited alloy showed a combination of adhesive and abrasive wear at low frequency and oxidative wear with deformation at the higher frequencies.

each alloy, the damage initiation point is highlighted in the supplementary figures. The critical load for damage initiation (L_C) was calculated according to Equation (3) and summarized in Table 1. The EMGs showed ~25–45% higher critical loads as compared to pure electrodeposited Ni. Among the EMGs, $Ni_{80}P_{20}$ showed the highest critical load for damage initiation of ~62 N.

Schematics for cohesive damage mechanism as a function of progressive load for the electrodeposited alloys are shown in Fig. 7, where $X_{(0)}$ indicate the critical length for damage initiation. The initial cohesion damage in case of pure electrodeposited Ni was mainly in the form of spallation within the wear scar (Fig. 7(a–b)). In certain regions, the alloy detached from the substrate on both sides of the groove which may be attributed to elastic recovery of the alloy behind the indenter that led to cohesive failure. Localized collapsing of the material was also seen, where the indenter tip penetrated the surface lowering the load bearing capacity of the alloy [44]. Fig. 7(c) shows the schematic of cohesive failure mechanism for $Ni_{90}P_{10}$ alloy characterized by arc tensile cracks during the initial stage of cohesive failure with a series of nested micro-cracks. SEM micrograph in Fig. 7(d) shows that the arc tensile cracks were mainly limited within the scratch groove and were not fully developed. The arc showed opening towards the direction of scratch and formed beyond the tip. These cracks indicate that the maximum tensile stress occurred at the trailing edge of the indenter [44]. A schematic of cohesive damage mechanism for $Ni_{85}P_{15}$ is shown in Fig. 7(e)

characterized by conformal/semi-circular cracks that expanded outside the grooves as clearly seen in the corresponding SEM image of the scratch groove in Fig. 7(f). Both angular cracks and developed conformal cracks were observed in this alloy. Similar type of failure has been reported previously for thermally sprayed TiN hard coatings [45]. The failure appeared to be more rounded as compared to arc tensile cracks and opened away from the scratch direction. Formation of semi-circular developed cracks may be due to stress exceeding the ultimate tensile strength and relatively low tensile ductility of the alloy [46]. Similar kind of failure mechanism was seen for $Ni_{80}P_{20}$ (schematic in Fig. 7(g)) with deep semi-circular/conformal cracks observed in the corresponding SEM micrograph of the scratch groove (Fig. 7(h)). In sum, $Ni_{90}P_{10}$ alloy showed ductile mode of cohesive failure while $Ni_{85}P_{15}$ and $Ni_{80}P_{20}$ alloys displayed relatively more brittle behavior. These findings are consistent with the nano-indentation results of Fig. 2(b), where high degree of serrations (or pop-ins) were observed for $Ni_{85}P_{15}$ and $Ni_{80}P_{20}$ indicating their brittle nature in contrast to the smooth load-displacement curve for $Ni_{90}P_{10}$ EMG supporting its relatively more ductile behavior. All the EMGs were in a tensile state of stress with very good interface bonding with the substrate and showed no signs of delamination after the scratch tests.

Wear rate versus hardness for various bulk metallic glasses (BMGs) [47–55] is shown in Fig. 8. In comparison to the bulk glasses, the Ni–P electrodeposited amorphous alloys investigated in this study showed
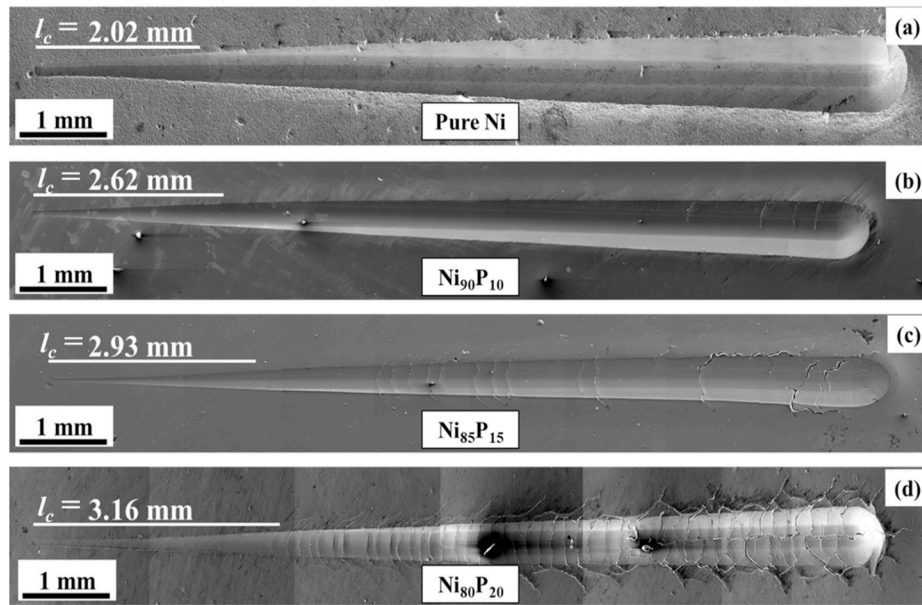
Fig. 6. SEM images of scratch scars showing the critical length at which crack initiated during progressive scratch test for (a) pure Ni, (b) $Ni_{90}P_{10}$, (c) $Ni_{85}P_{15}$, and (d) $Ni_{80}P_{20}$.
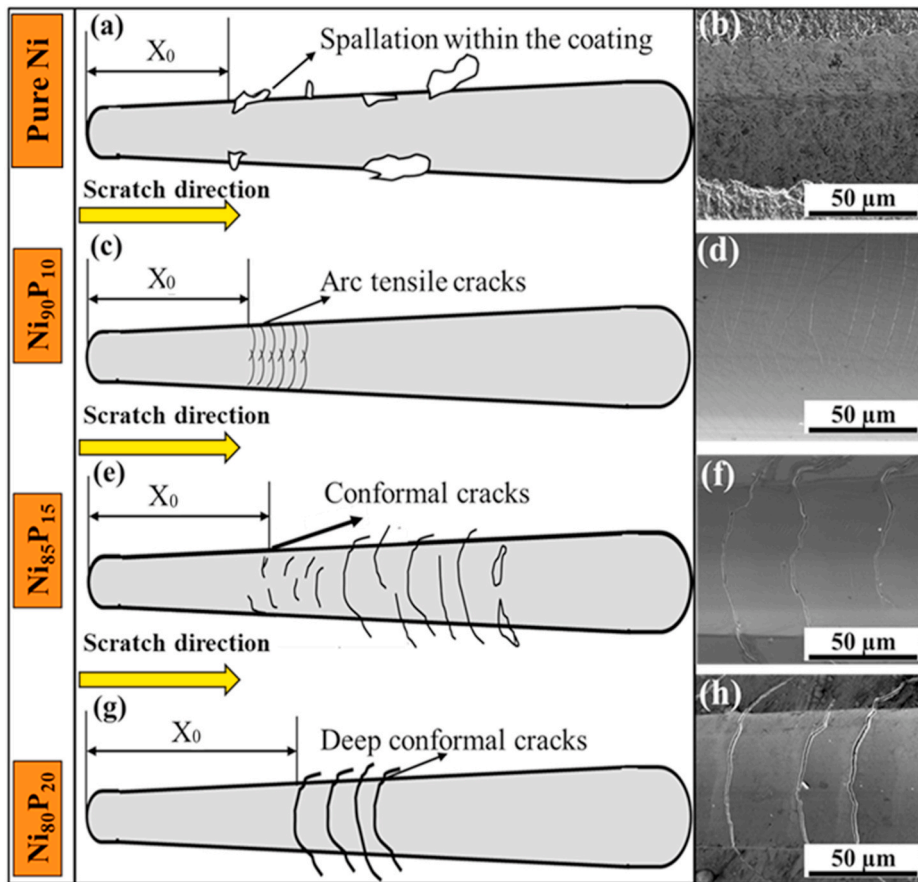

Fig. 7. Schematic and SEM image showing cohesive failure mechanisms for the electrodeposited alloys from progressive scratch tests, where X_0 indicate the critical length for crack initiation: (a, b) pure Ni showed localized collapse of material and spallation; (c, d) $Ni_{90}P_{10}$ showed damage in the form of arc tensile cracks under the moving indenter indicating ductile nature; (e, f) $Ni_{85}P_{15}$ showed angular/semicircular cracks at the scratch groove edge; (g, h) $Ni_{80}P_{20}$ showed deep angular/semicircular cracks indicating brittle nature.

excellent wear resistance at relatively lower hardness. Wear volume loss (V_w) and wear rate (W_R) are inversely proportional to the hardness (H), as represented by Archard's relationship in equations (4) and (5) and shown schematically by the dashed line in Fig. 8:

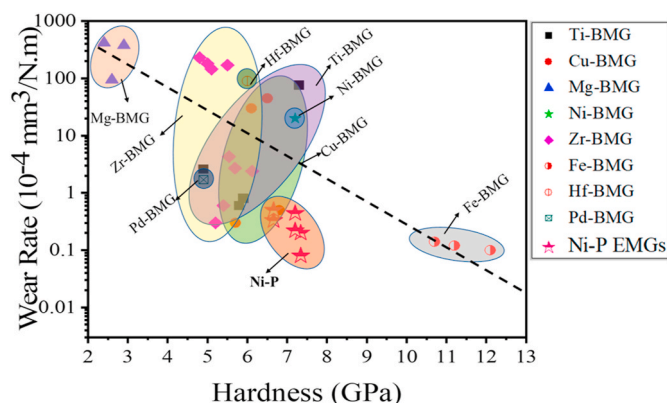$$V_w = k\frac{s.N}{H} \tag{4}$$

$$W_R = \frac{k}{H} \tag{5}$$

Fig. 8. Wear rate versus hardness of representative bulk metallic glasses (BMGs) studied under dry sliding conditions [47–55] in comparison with the Ni–P electrodeposited metallic glasses (EMGs) developed in this study.

where, k is the dimensionless wear coefficient, s is the sliding distance, and N is the applied load [56]. Mg-based BMGs exhibited some of the highest wear rates while Fe-based BMGs showed the lowest wear rates among the reported alloys [51,55]. For some BMGs, wear rate has been found to be hardness dependent while others show significant deviation from this relationship suggesting other mechanisms in play including the underlying fracture behavior [50,52,55]. The predominant wear mechanism of viscous flow along with discontinuous transfer film for Zr- and Ti- based BMGs increased their wear rates [52]. In contrast, the primary wear mechanisms for the Ni–P EMGs was found to be oxidative wear and plastic deformation. In comparison to BMGs, the Ni–P EMGs developed in the present study showed some of the lowest wear rates, which may be related to the high H/E and H^3/E^2 values that are indicative of high fracture toughness for these electrodeposited alloys together with the distinctly different wear mechanism.

4. Conclusions

The sliding wear and scratch behavior of electrodeposited Ni and Ni–P alloys were studied systematically as a function of composition. The following main conclusions may be drawn from this study:

1. Amorphous alloy formation was seen in the case of $Ni_{100-x}P_x$ system by electrodeposition for phosphorus content (x) in the narrow range of 10–20 at. %.
2. A three-fold higher hardness was observed for the electrodeposited Ni–P metallic glasses, namely $Ni_{80}P_{20}$, $Ni_{85}P_{15}$, and $Ni_{90}P_{10}$, as compared to pure electrodeposited Ni. Nanoindentation load-displacement curves showed high degree of serrations (or pop-ins) for $Ni_{85}P_{15}$ and $Ni_{80}P_{20}$ indicating their brittle nature in contrast to smooth load-displacement curve for $Ni_{90}P_{10}$ supporting its ductile behavior.
3. Coefficient of friction and wear rates were lower for the electrodeposited metallic glasses as compared to pure Ni. Among the electrodeposited metallic glasses, wear rate decreased in the order: $Ni_{90}P_{10} > Ni_{85}P_{15} > Ni_{80}P_{20}$, which was attributed to the increase in hardness (H), H/E, and H^3/E^2 values with higher phosphorus content.
4. The wear mechanism was studied as a function of load and frequency. For the electrodeposited metallic glasses, there was a transition from mild abrasion to oxidative wear and plastic deformation with increase in load and frequency. In contrast, a transition from abrasive to oxidative wear with severe delamination was observed for electrodeposited pure Ni with increase in load and frequency.
5. Progressive scratch response showed an increase in critical load to initial failure with increase in phosphorus content. The $Ni_{80}P_{20}$ alloy

showed the highest load to critical failure with average value of about 62 N among the studied alloys.
6. The cohesive failure mechanism was observed to be spallation in case of electrodeposited pure Ni in contrast to conformal/developed semicircular cracks for the electrodeposited metallic glasses.

CRediT authorship contribution statement

Mayur Pole: Formal analysis, Investigation, Writing – original draft. **Maryam Sadeghilaridjani:** Investigation, Writing – original draft. **Jibril Shittu:** Formal analysis, Investigation. **Chaitanya Mahajan:** Formal analysis, Investigation. **Nandita Ghodki:** Formal analysis, Investigation. **Sundeep Mukherjee:** Conceptualization, Investigation, Resources, Supervision, Project administration, Writing – review & editing.

Declaration of competing interest

The authors declare that they have no conflict of interest that could have appeared to influence the work reported in this paper.

Acknowledgments

Appendix A. Supplementary data

Supplementary data to this article can be found online at https://doi.org/10.1016/j.msea.2021.141315.

References

[1] A.L. Greer, K.L. Rutherford, I.M. Hutchings, Wear resistance of amorphous alloys and related materials, Int. Mater. Rev. 47 (2002) 87–112, https://doi.org/10.1179/095066001225001067.

[2] A. Inoue, Stabilization of metallic supercooled liquid and bulk amorphous alloys, Acta Mater. 48 (2000) 279–306, https://doi.org/10.1016/S1359-6454(99)00300-6.

[3] P.H. Cornuault, G. Colas, A. Lenain, R. Daudin, S. Gravier, On the diversity of accommodation mechanisms in the tribology of Bulk Metallic Glasses, Tribol. Int. 141 (2020), https://doi.org/10.1016/j.triboint.2019.105957.

[4] M. Sadeghilaridjani, A. Ayyagari, S. Muskeri, V. Hasannaeimi, J. Jiang, S. Mukherjee, Small-Scale mechanical behavior of ion-irradiated bulk metallic glass, JOM (J. Occup. Med.) 72 (2020) 123–129, https://doi.org/10.1007/s11837-019-03848-3.

[5] H.S. Arora, Q. Xu, Z. Xia, Y.H. Ho, N.B. Dahotre, J. Schroers, S. Mukherjee, Wettability of nanotextured metallic glass surfaces, Scripta Mater. 69 (2013) 732–735, https://doi.org/10.1016/j.scriptamat.2013.08.014.

[6] H.S. Arora, H.S. Grewal, H. Singh, S. Mukherjee, Zirconium based bulk metallic glass-Better resistance to slurry erosion compared to hydroturbine steel, Wear 307 (2013) 28–34, https://doi.org/10.1016/j.wear.2013.08.016.

[7] D.C. Hofmann, R. Polit-Casillas, S.N. Roberts, J.P. Borgonia, R.P. Dillon, E. Hilgemann, J. Kolodziejska, L. Montemayor, J.O. Suh, A. Hoff, K. Carpenter, A. Parness, W.L. Johnson, A. Kennett, B. Wilcox, Castable bulk metallic glass strain wave gears: towards decreasing the cost of high-performance robotics, Sci. Rep. 6 (2016) 1–11, https://doi.org/10.1038/srep37773.

[8] D.C. Hofmann, L.M. Andersen, J. Kolodziejska, S.N. Roberts, J.P. Borgonia, W. L. Johnson, K.S. Vecchio, A. Kennett, Optimizing bulk metallic glasses for robust, highly wear-resistant gears, Adv. Eng. Mater. 19 (2017) 1–10, https://doi.org/10.1002/adem.201600541.

[9] D.V. Louzguine-Luzgin, M. Ito, S.V. Ketov, A.S. Trifonov, J. Jiang, C.L. Chen, K. Nakajima, Exceptionally high nanoscale wear resistance of a Cu47Zr45Al8 metallic glass with native and artificially grown oxide, Intermetallics 93 (2018) 312–317, https://doi.org/10.1016/j.intermet.2017.10.011.

[10] M. Sadeghilaridjani, Y.C. Yang, V. Hasannaeimi, C. Mahajan, S. Jha, M. Pole, Z. Xia, S. Mukherjee, Multiscale manufacturing of amorphous alloys by a facile electrodeposition approach and their property dependence on the local atomic order, ACS Appl. Mater. Interfaces 13 (2021) 9260–9271, https://doi.org/10.1021/acsami.0c22153.

[11] V. Hasannaeimi, X. Wang, R. Salloom, Z. Xia, J. Schroers, S. Mukherjee, Nanomanufacturing of non-noble amorphous alloys for electrocatalysis, ACS Appl. Energy Mater. 3 (2020) 12099–12107, https://doi.org/10.1021/acsaem.0c02221.

[12] H. Capel, P.H. Shipway, S.J. Harris, Sliding wear behaviour of electrodeposited cobalt-tungsten and cobalt-tungsten-iron alloys, Wear 255 (2003) 917–923, https://doi.org/10.1016/S0043-1648(03)00241-2.

[13] H. Wang, S. Yao, S. Matsumura, Preparation, characterization and the study of the thermal strain in Ni-W gradient deposits with nanostructure, Surf. Coating. Technol. 157 (2002) 166–170, https://doi.org/10.1016/S0257-8972(02)00151-2.

[14] S. Eskin, O. Berkh, G. Rogalsky, J. Zahavi, Co-W alloys for replacement of conventional hard chromium, plat, Surf. Finish. 85 (1998) 79–83.

[15] P. Sampath Kumar, P. Kesavan Nair, Studies on crystallization of electroless Ni-P deposits, J. Mater. Process. Technol. 56 (1996) 511–520, https://doi.org/10.1016/0924-0136(96)85110-7.

[16] J.Y. Song, J. Yu, Residual stress measurements in electroless plated Ni-P films, Thin Solid Films 415 (2002) 167–172, https://doi.org/10.1016/S0040-6090(02)00556-4.

[17] M. Palaniappa, S.K. Seshadri, Friction and wear behavior of electroless Ni-P and Ni-W-P alloy coatings, Wear 265 (2008) 735–740, https://doi.org/10.1016/j.wear.2008.01.002.

[18] S. Alirezaei, S.M. Monirvaghefi, M. Salehi, A. Saatchi, Wear behavior of Ni-P and Ni-P-Al2O3 electroless coatings, Wear 262 (2007) 978–985, https://doi.org/10.1016/j.wear.2006.10.013.

[19] L. Wang, Y. Gao, Q. Xue, H. Liu, T. Xu, A novel electrodeposited Ni-P gradient deposit for replacement of conventional hard chromium, Surf. Coating. Technol. 200 (2006) 3719–3726, https://doi.org/10.1016/j.surfcoat.2004.10.016.

[20] T.R. Tamilarasan, R. Rajendran, M. Siva shankar, U. Sanjith, G. Rajagopal, J. Sudagar, Wear and scratch behaviour of electroless Ni-P-nano-TiO2: effect of surfactants, Wear 346–347 (2016) 148–157, https://doi.org/10.1016/j.wear.2015.11.015.

[21] K.H. Hou, M.C. Jeng, M. Der Ger, A study on the wear resistance characteristics of pulse electroforming Ni-P alloy coatings as plated, Wear 262 (2007) 833–844, https://doi.org/10.1016/j.wear.2006.08.023.

[22] T. Nakanishi, M. Ozaki, H.-S. Nam, T. Yokoshima, T. Osaka, Pulsed electrodeposition of nanocrystalline CoNiFe soft magnetic thin films, J. Electrochem. Soc. 148 (2001) C627, https://doi.org/10.1149/1.1388886.

[23] J.J. Kelly, M. Cantoni, D. Landolt, Three-dimensional structuring of electrodeposited Cu-Co multilayer alloys, J. Electrochem. Soc. 148 (2001) C620, https://doi.org/10.1149/1.1388629.

[24] H.S. Chen, Glassy metals, Reports Prog. Phys. Rev. 43 (1980) 353.

[25] M.T. Pace, R.C. Thomson, J. Wells, W. Peterson, J.E. Gould, D.J. Barnes, American society for testing and materials, S. Paul, ASTM C1624-05: standard test method for adhesion strength and mechanical failure modes of ceramic by quantitative single point scratch testing, coatings, 2015, pp. 1–29, https://doi.org/10.1520/C1624-05R15.Scope, 05.

[26] A.L. Greer, Y.Q. Cheng, E. Ma, Shear bands in metallic glasses, Mater. Sci. Eng. R Rep. 74 (2013) 71–132, https://doi.org/10.1016/j.mser.2013.04.001.

[27] C.A. Schuh, A.C. Lund, T.G. Nieh, New regime of homogeneous flow in the deformation map of metallic glasses: elevated temperature nanoindentation experiments and mechanistic modeling, Acta Mater. 52 (2004) 5879–5891, https://doi.org/10.1016/j.actamat.2004.09.005.

[28] J.G. Wang, B.W. Choi, T.G. Nieh, C.T. Liu, Crystallization and nanoindentation behavior of a bulk Zr–Al–Ti–Cu–Ni amorphous alloy, J. Mater. Res. 15 (2000) 798–807, https://doi.org/10.1557/JMR.2000.0114.

[29] J. Cheng, D. Liu, X. Liang, Y. Chen, Surface & Coatings Technology Evolution of microstructure and mechanical properties of in situ synthesized TiC – TiB 2/ CoCrCuFeNi high entropy alloy coatings, Surf. Coating. Technol. 281 (2015) 109–116, https://doi.org/10.1016/j.surfcoat.2015.09.049.

[30] H.L. Costa, M.M.O. Junior, J.D.B. De Mello, Effect of debris size on the reciprocating sliding wear of aluminium, Wear 376–377 (2017) 1399–1410, https://doi.org/10.1016/j.wear.2016.10.025.

[31] J.L. Mo, M.H. Zhu, A. Leyland, A. Matthews, Impact wear and abrasion resistance of CrN, AlCrN and AlTiN PVD coatings, Surf. Coating. Technol. 215 (2013) 170–177, https://doi.org/10.1016/j.surfcoat.2012.08.077.

[32] J Mushil, Tribological and mechanical properties of nanocrystalline-TiC/a-Cnanocrystalline-TiC/a-C nanocomposite thin films, J. Vac. Sci. Technol. A 28 (2010) 244, https://doi.org/10.1116/1.3294717. AVS.

[33] A. Fernández, Fl uence of the microstructure on the mechanical and tribological behavior of TiC/a-C nanocomposite coatings, Thin Solid Films 517 (2009) 1656–1665, https://doi.org/10.1016/j.tsf.2008.09.091.

[34] D. Galvan, Y.T. Pei, J.T.M. De Hosson, Deformation and failure mechanism of nano-composite coatings under nano-indentation 200 (2006) 6718–6726, https://doi.org/10.1016/j.surfcoat.2005.10.010.

[35] J. Musil, Hard and Superhard Nanocomposite Coatings. Surface and Coatings Technology 125, Elsevier, 2000, pp. 322–330, https://doi.org/10.1016/S0257-8972(99)00586-1.

[36] W. Ames, A.T. Alpas, Wear mechanisms in hybrid composites of graphite-20 pct SiC in A356 aluminum alloy (Al-7 pct Si-0 . 3 pct Mg), Metall. Mater. Trans. 26 (1995), https://doi.org/10.1007/BF02669796.

[37] C.S. Ramesh, S.K. Seshadri, Tribological characteristics of nickel based composite coatings, Wear 255 (2003) 893–902, https://doi.org/10.1016/S0043-1648(03)00080-2.

[38] C.N. Panagopoulos, P.E. Agathocleous, V.D. Papachristos, A. Michaelides, Sliding wear behaviour of zinc – iron alloy electrodeposits, Surf. Coating. Technol. 123 (2000) 62–71, https://doi.org/10.1016/S0257-8972(99)00469-7.

[39] M. Roy, A. Pauschitz, R. Polak, F. Franek, Comparative evaluation of ambient temperature friction behaviour of thermal sprayed Cr3C2-25(Ni20Cr) coatings with conventional and nano-crystalline grains, Tribol. Int. 39 (2006) 29–38, https://doi.org/10.1016/j.triboint.2004.11.009.

[40] A. Caron, P. Sharma, A. Shluger, H. Fecht J, D. Louzguine-Luzguin, A. Inoue, Effect of surface oxidation on the nm-scale wear behavior of a metallic glass, J. Appl. Phys. 109 (2011), https://doi.org/10.1063/1.3573778.

[41] C.S. Ramesh, R. Keshavamurthy, B.H. Channabasappa, S. Pramod, Friction and wear behavior of Ni-P coated Si3N4 reinforced Al6061 composites, Tribol. Int. 43 (2010) 623–634, https://doi.org/10.1016/j.triboint.2009.09.011.

[42] A. Caron, P. Sharma, A. Shluger, H.J. Fecht, D.V. Louzguine-Luzguin, A. Inoue, Effect of surface oxidation on the nm-scale wear behavior of a metallic glass, J. Appl. Phys. 109 (2011), https://doi.org/10.1063/1.3573778.

[43] S.J. Kang, K.T. Rittgen, S.G. Kwan, H.W. Park, R. Bennewitz, A. Caron, Importance of surface oxide for the tribology of a Zr-based metallic glass, Friction 5 (2017) 115–122, https://doi.org/10.1007/s40544-017-0149-7.

[44] A. Ghabchi, S. Sampath, K. Holmberg, T. Varis, Damage mechanisms and cracking behavior of thermal sprayed WC-CoCr coating under scratch testing, Wear 313 (2014) 97–105, https://doi.org/10.1016/j.wear.2014.02.017.

[45] S.J. Bull, Failure mode maps in the thin film scratch adhesion test, Tribol. Int. 30 (1997) 491–498, https://doi.org/10.1016/S0301-679X(97)00012-1.

[46] B. Prakash, Abrasive wear behaviour of Fe, Co and Ni based metallic glasses, Wear 258 (2005) 217–224, https://doi.org/10.1016/j.wear.2004.09.010.

[47] J. Kong, D. Xiong, J. Li, Q. Yuan, R. Tyagi, Effect of flash temperature on tribological properties of bulk metallic glasses, Tribol. Lett. 35 (2009) 151–158, https://doi.org/10.1007/s11249-009-9444-4.

[48] Y. Huang, H. Fan, D. Wang, Y. Sun, F. Liu, J. Shen, J. Sun, J. Mi, The effect of cooling rate on the wear performance of a ZrCuAlAg bulk metallic glass, Mater. Des. 58 (2014) 284–289, https://doi.org/10.1016/j.matdes.2014.01.067.

[49] L. Liu, C.L. Qiu, C.Y. Huang, Y. Yu, H. Huang, S.M. Zhang, Biocompatibility of Ni-free Zr-based bulk metallic glasses, Intermetallics 17 (2009) 235–240, https://doi.org/10.1016/j.intermet.2008.07.022.

[50] G.Q. Zhang, X.J. Li, M. Shao, L.N. Wang, J.L. Yang, L.P. Gao, L.Y. Chen, C.X. Liu, Wear behavior of a series of Zr-based bulk metallic glasses, Mater. Sci. Eng. 475 (2008) 124–127, https://doi.org/10.1016/j.msea.2007.05.039.

[51] Z. Liao, N. Hua, W. Chen, Y. Huang, T. Zhang, Correlations between the wear resistance and properties of bulk metallic glasses, Intermetallics 93 (2018) 290–298, https://doi.org/10.1016/j.intermet.2017.10.008.

[52] E. Fleury, S.M. Lee, H.S. Ahn, W.T. Kim, D.H. Kim, Tribological properties of bulk metallic glasses, Mater. Sci. Eng. 375–377 (2004) 276–279, https://doi.org/10.1016/j.msea.2003.10.065.

[53] M.L. Rahaman, L. Zhang, M. Liu, W. Liu, Surface roughness effect on the friction and wear of bulk metallic glasses, Wear 332–333 (2015) 1231–1237, https://doi.org/10.1016/j.wear.2014.11.030.

[54] D.R. Maddala, A. Mubarok, R.J. Hebert, Sliding wear behavior of Cu50Hf41.5Al8.5 bulk metallic glass, Wear 269 (2010) 572–580, https://doi.org/10.1016/j.wear.2010.06.004.

[55] D.R. Maddala, R.J. Hebert, Sliding wear behavior of Fe 50-xCr 15Mo 14C 15B 6Er x (x=0, 1, 2at%) bulk metallic glass, Wear 294–295 (2012) 246–256, https://doi.org/10.1016/j.wear.2012.06.007.

[56] J.F. Archard, W. Hirst, The wear of metals under unlubricated conditions, Proc. R. Soc. London. Ser. A Math. Phys. Sci. 236 (1956) 397–410, https://doi.org/10.1098/rspa.1956.0144.